Spatial beam dynamics in graded-index multimode fibers under Raman amplification: A variational approach

Ashis Paul [1,*] Anuj P. Lara [1,*] Samudra Roy, [1,†] and Govind P. Agrawal [2]
[1] *Department of Physics, Indian Institute of Technology Kharagpur, West Bengal 721302, India*
[2] *Institute of Optics, University of Rochester, Rochester, New York 14627, USA*

We investigate the spatial beam dynamics inside a multimode graded-index fiber under Raman amplification by adopting a semianalytical variational approach. The variational analysis provides us with four coupled ordinary differential equations that govern the beam's evolution and are much faster to solve numerically compared to the full nonlinear wave equation. Their solution also provides considerable physical insight and allows us to study the impact of important nonlinear phenomena such as self-focusing and cross-phase modulation. We first show that the variational results agree well with full numerical simulations over a wide range of operating parameters. We use them to investigate the signal beam's amplification for different initial widths of the pump and signal beams. This allows us to quantify the pumping conditions under which the quality of a signal beam could be improved at the fiber's output end. Our analysis may prove beneficial in practice for two reasons. First, it can be used to scan the design parameters of an experiment in a time-efficient fashion and determine the optimum values of these parameters. Second, it can provide physical insight into nonlinear phenomena involved in the Raman-amplification process.

I. INTRODUCTION

The quest for higher and higher output powers has led to the use of multimode fibers for fiber-based lasers and amplifiers [1–3]. In recent years, graded-index (GRIN) multimode fibers have replaced traditional step-index fibers for making high-power Raman amplifiers. This is motivated by a phenomenon known as the Raman-induced spatial beam cleanup [4–8], which considerably improves the amplified signal's beam quality at the output end of a Raman amplifier. Recent experiments have shown that power levels of more than 2 kW can be realized using GRIN fibers for Raman amplification [9–11].

The use of a mode-based approach for understanding the Raman-induced spatial beam cleanup becomes less appropriate when many modes of a GRIN fiber are excited by the incoming pump and signal beams. A nonmodal numerical approach was recently proposed for both Yb-doped fiber amplifiers [12] and Raman GRIN amplifiers [8] that takes into account most relevant physical effects under continuous-wave (cw) diode pumping. However, such an extensive numerical model is time consuming because it requires a solution of the coupled nonlinear partial differential equations satisfied by the pump and signal beams. Recent work on Kerr-induced beam cleaning [13,14] has shown that the phenomenon of periodic self-imaging [15], a unique property of GRIN fibers, plays an important role in the amplification of the signal beam by creating a nonlinear index grating inside the GRIN fiber. Simple analytic models based on self-imaging have been proposed

recently to study amplification and beam narrowing in GRIN fibers [16,17]. However, these models did not include all the important nonlinear effects such as self-phase modulation (SPM) and cross-phase modulation (XPM).

In this work we apply the variational method to develop a semianalytic model of the Raman-amplification process in GRIN-fiber amplifiers. We solve the resulting equations numerically to investigate the impact of both SPM and XPM on the performance of a Raman amplifier. In our treatment, the Gaussian profile of the pump is not approximated with a parabolic shape, which may produce erroneous results. We show that our semianalytic approach is much less computationally time consuming compared to a fully numerical approach, while providing reasonably accurate results over a wide range of operating parameters. Its use is beneficial in practice for two reasons. First, it can be used to scan the design parameters of an experiment in a time-efficient fashion and determine the optimum values of these parameters. Second, it can provide physical insight into different nonlinear phenomena involved in the Raman-amplification process.

The article is organized as follows. In Sec. II we outline the theory that leads to the nonlinear coupled propagation equations for the pump and signal beams. In Sec. III we develop the variational analysis by forming a suitable Lagrangian and derive four coupled ordinary differential equations describing the signal beam's dynamics under the Raman gain. We compare the variational results with full numerical simulations and show the robustness of our approach. In Sec. IV we solve numerically the coupled equations for the signal beam's parameters and investigate its dynamics and stability under the impact of SPM and XPM for different initial conditions. The main conclusions are summarized in Sec. V.

---

*These authors have contributed equally to this work.
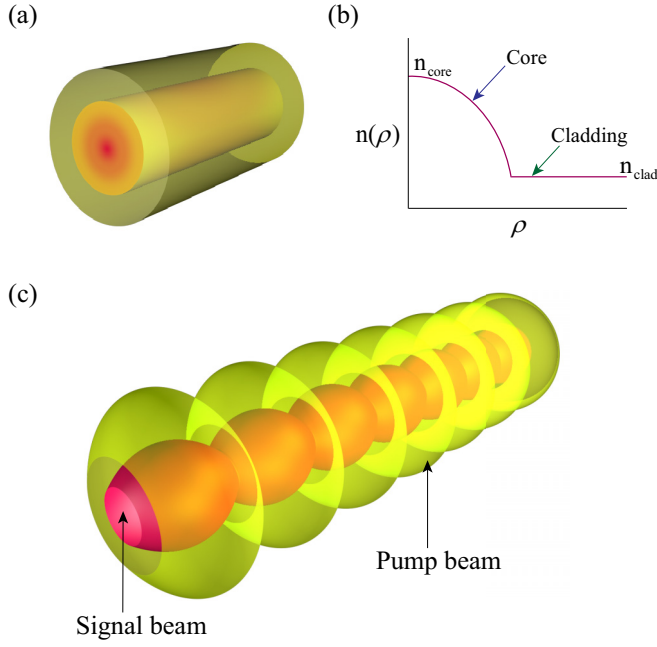†samudra.roy@phy.iitkgp.ac.in

FIG. 1. (a) Schematic of a GRIN fiber and (b) its parabolic index profile. (c) Two isosurfaces showing how the signal and pump beams evolve in a periodic fashion inside a GRIN fiber because of the self-imaging provided by the parabolic index profile.

II. THEORY

We consider a GRIN fiber with a parabolic refractive index profile [see Figs. 1(a) and 1(b)] and include the optical Kerr effect using

$$n(\rho) = n_{\text{core}}(1 - \tfrac{1}{2}b^2\rho^2) + n_2|E|^2, \quad (1)$$

where $\rho = \sqrt{x^2 + y^2}$ is the radial distance from the central axis of the GRIN fiber and n_{core} is the refractive index at $\rho = 0$. The index gradient b is defined as $b = \sqrt{2\Delta}/a$, where a is the core's radius of the GRIN fiber and Δ is the relative core-cladding index difference defined as $\Delta = (n_{\text{core}} - n_{\text{clad}})/n_{\text{core}}$. The Kerr coefficient n_2 and has a value of 2.7×10^{-20} m²/W for silica fibers. In practice, silica molecules also produce a noninstantaneous response in addition to the nearly instantaneous Kerr response of electrons. This response, known as the Raman response, is delayed in time. It is accounted for by modifying the Kerr term $n_2|E|^2$ in Eq. (1) as [18]

$$n_2|E|^2 = (1 - f_R)n_2|E|^2 + f_R n_2 \int_0^\infty h_R(t')|E(t - t')|^2 dt', \quad (2)$$

where f_R is the fractional Raman contribution (about 18% for silica fibers) and $h_R(t) = (\tau_1^{-2} + \tau_2^{-2})\tau_1 \exp(-t/\tau_2)\sin(t/\tau_1)$ is the Raman response function, with $\tau_{j=1,2}$ being two constants. The response function is normalized with $\int_0^\infty h_R(t)dt = 1$.

The pump and signal beams are launched at the input end of the GRIN fiber located at $z = 0$. The total electric field $E(\mathbf{r}, t)$ inside the fiber at a distance z can be written as

$$E(\mathbf{r}, t) = A_p \exp[i(k_p z - \omega_p t)] + A_s \exp[i(k_s z - \omega_s t)], \quad (3)$$

where $A_j(\rho, z)$ and $k_j = n_{\text{core}}(\omega_j)\omega_j/c$, with $j = p, s$, are the amplitudes and wave numbers of pump and signal beams, respectively. Both waves are assumed to be polarized in the same direction. In our simulations, we choose the wavelengths for the pump (λ_p) and signal (λ_s) beams to be 1018 and 1060 nm, respectively, and use $\Omega = \omega_p - \omega_s$ for the frequency shift of the signal from the pump. Using Eq. (3), we evaluate the integral in Eq. (2) to obtain

$$\int_0^\infty h_R(t')|E(t - t')|^2 dt' = |A_p|^2 + |A_s|^2 + A_p^* A_s e^{-i\delta k z}\tilde{h}_R(\Omega)$$
$$+ A_p A_s^* e^{i\delta k z}\tilde{h}_R^*(\Omega), \quad (4)$$

where $\delta k = k_p - k_s$ and $\tilde{h}_R(\Omega)$ is the Fourier transform of $h_R(t)$. The Raman gain coefficient g_R is related to the imaginary part of $\tilde{h}_R(\Omega)$ as $g_R = 2f_R n_2(\omega_s/c)\text{Im}(\tilde{h}_R)$.

Using Eqs. (2)–(4) in Maxwell's equations and retaining only the phase-matched terms under the slowly varying envelope approximation, we can separate the pump and signal terms and obtain two coupled nonlinear equations for the pump and signal amplitudes [16],

$$\frac{\partial A_p}{\partial z} + \frac{\nabla_\perp^2 A_p}{2ik_p} + \frac{i}{2}k_p b^2 \rho^2 A_p = \frac{i\omega_p}{c}n_2|A_p|^2 A_p, \quad (5)$$

$$\frac{\partial A_s}{\partial z} + \frac{\nabla_\perp^2 A_s}{2ik_s} + \frac{i}{2}k_s b^2 \rho^2 A_s = \frac{i\omega_s}{c}n_2(|A_s|^2 + 2|A_p|^2)A_s$$
$$+ \frac{1}{2}g_R|A_p|^2 A_s, \quad (6)$$

where $\nabla_\perp^2 = \frac{1}{\rho}\frac{\partial}{\partial\rho}(\rho\frac{\partial}{\partial\rho}) + \frac{1}{\rho^2}\frac{\partial^2}{\partial\phi^2}$ is the transverse Laplacian. Here we have neglected the depletion and XPM terms in the pump equation (5), assuming the pump to remain much more intense than the signal over the entire length of the GRIN fiber. As a result, this equation can be solved first to obtain $A_p(\rho, z)$. For a cw pump in the form of a Gaussian beam, Eq. (5) has been solved with the variational method and the solution is given as [19]

$$A_p(\rho, z) = \sqrt{\frac{I_{p0}}{f_p(z)}}\exp\left(-\frac{\rho^2}{2w_{p0}^2 f_p(z)} + i\Theta(\rho, z)\right), \quad (7)$$

where I_{p0} is the peak intensity and w_{p0} is the width of the input pump beam at $z = 0$, while the periodic function $f_p(z)$ is defined as

$$f_p(z) = \cos^2(bz) + C_p^2 \sin^2(bz), \quad C_p = \sqrt{1 - p}/bk_p w_{p0}^2, \quad (8)$$

with $p = P_{p0}/P_c$. Here $P_{p0} = \pi w_{p0}^2 I_{p0}$ is the input pump power and $P_c = 2\pi n_{\text{core}}/n_2 k_p^2$ is the critical power at which the pump beam collapses due to self-focusing. Because of GRIN-induced self-imaging, the pump beam compresses and expands periodically such that it recovers its input shape and width at distances $z = m\pi/b = mz_p$, where m is an integer and z_p is the period. Thus, in normalized units the self-imaging period becomes $\xi_p = z_p b = \pi$. Figure 1(c) shows schematically the periodic evolution of such a pump beam inside the GRIN fiber.

III. VARIATIONAL ANALYSIS

Exploiting the analytical pump solution given in Eq. (7), we can numerically solve the signal equation in Eq. (6). However, numerical simulations become time consuming for distances exceeding the 10 m required for Raman amplifiers. A numerical approach also hinders physical insight and does not reveal what parameters are most relevant for the narrowing of the signal beam to occur. To gain insight into how the SPM, XPM, and Raman phenomena affect the signal beam, we adopt the variational method [20] for solving Eq. (6). The variational method has been used successfully, in spite of the gain and loss terms that make the underlying system nonconservative [21]. It requires a suitable ansatz for the pulse shape and makes the assumption that the functional form of the pulse shape remains intact in the presence of small perturbations, but its parameters appearing in the ansatz (amplitude, width, position, phase, frequency, etc.) evolve with propagation.

First, we normalize Eq. (6) and rewrite it in the form

$$i\frac{\partial \psi_s}{\partial \xi} + \frac{\delta}{2}\left(\frac{\partial^2 \psi_s}{\partial r^2} + \frac{1}{r}\frac{\partial \psi_s}{\partial r}\right) - \frac{1}{2\delta}r^2\psi_s + \gamma|\psi_s|^2\psi_s$$

$$= -2\Gamma|\psi_p|^2\psi_s + i\frac{G_R}{2}|\psi_p|^2\psi_s, \quad (9)$$

where the variables are scaled using $\xi = bz$, $r = \rho/w_{s0}$, and $\psi_j = A_j/\sqrt{I_{j0}}$, with $j = s, p$. Here w_{s0} is the width and I_{s0} is the peak intensity of the input signal beam, $\delta = w_g^2/w_{s0}^2$ is a dimensionless ratio, and $w_g^2 = 1/bk_s$ is the width of the fundamental mode of the GRIN fiber at the signal's frequency ω_s. Typically, w_g is close to 5 μm for GRIN fibers. The other parameters, namely, $\gamma = \omega_s n_2 I_{s0}/cb$, $\Gamma = \omega_s n_2 I_{p0}/cb$, and $G_R = g_R I_{p0}/b$, are the normalized SPM, XPM, and Raman coefficients, respectively. To implement the variational method, we treat the two terms on the right-hand side of Eq. (9) as a small perturbation ϵ, defined such that

$$\epsilon = \left(2i\Gamma + \tfrac{1}{2}G_R\right)|\psi_p|^2\psi_s. \quad (10)$$

The Lagrangian density $\mathcal{L}_d$ corresponding to Eq. (9) has the form [22]

$$\mathcal{L}_d = \frac{i}{2}r(\psi_s\partial_\xi\psi_s^* - \psi_s^*\partial_\xi\psi_s) + \frac{\delta}{2}r|\partial_r\psi_s|^2$$

$$- \frac{\gamma}{2}r|\psi_s|^4 + \frac{r^3}{2\delta}|\psi_s|^2 + ir(\epsilon\psi_s^* - \epsilon^*\psi_s), \quad (11)$$

where $\partial_{j=\xi,r} \equiv \partial/\partial j$. We choose a chirped Gaussian beam for our ansatz for ψ_s because the signal is often in the form of a Gaussian beam in practice,

$$\psi_s(r,\xi) = \psi_{s0}(\xi)\exp\left(-\frac{r^2}{2r_s^2(\xi)} + id_s(\xi)r^2 + i\phi_s(\xi)\right), \quad (12)$$

where the four parameters ψ_{s0}, r_s, d_s, and ϕ_s represent the amplitude, width, phase-front curvature, and phase, respectively, and depend on ξ. The normalized signal width r_s is defined as $r_s(\xi) = w_s(\xi)/w_{s0}$. Using this ansatz and following the standard Rayleigh-Ritz optimization procedure [22], we obtain the reduced Lagrangian $L = \int_0^\infty \mathcal{L}_d \, dr$ by integrating

over r. The result is found to be

$$L = \frac{1}{2}\psi_{s0}^2 r_s^2\left(\frac{d\phi_s}{d\xi}\right) + \left(2\delta d_s^2 + \frac{1}{2\delta} + \frac{dd_s}{d\xi}\right)\frac{\psi_{s0}^2 r_s^4}{2}$$

$$+ \frac{\delta}{4}\psi_{s0}^2 - \frac{\gamma}{8}\psi_{s0}^4 r_s^2 + i\int_0^\infty r(\epsilon\psi_s^* - \epsilon^*\psi_s)dr. \quad (13)$$

We evaluate the integral in Eq. (13) by using the pump intensity from Eq. (7). The normalized form of this intensity is

$$|\psi_p(\xi)|^2 = f_p(\xi)^{-1}\exp\left[-r^2/r_{p0}^2 f_p(\xi)\right], \quad (14)$$

where $r_{p0} = w_{p0}/w_{s0}$ is the normalized width of the input pump beam.

We now use the Euler-Lagrange equation $\partial_\xi(\partial_{X_\xi}L) - \partial_X L = 0$, with $X = \psi_{s0}, r_s, d_s, \phi_s$, and obtain the four coupled equations for the evolution of the four parameters along the amplifier's length,

$$\frac{d\psi_{s0}}{d\xi} = -2\delta d_s\psi_{s0} + \frac{G_R}{2f_p}\left(\frac{r_e}{r_s}\right)^2\left[2 - \left(\frac{r_e}{r_s}\right)^2\right]\psi_{s0}, \quad (15)$$

$$\frac{dr_s}{d\xi} = 2\delta d_s r_s - \frac{G_R}{2f_p}\left(\frac{r_e}{r_s}\right)^2\left[1 - \left(\frac{r_e}{r_s}\right)^2\right]r_s, \quad (16)$$

$$\frac{dd_s}{d\xi} = -2\delta d_s^2 - \frac{\gamma}{4}\left(\frac{\psi_{s0}}{r_s}\right)^2 - \frac{1}{2\delta} + \frac{\delta}{2r_s^4}$$

$$- \frac{2\Gamma}{f_p}\left(\frac{r_e^2}{r_s^4}\right)\left[1 - \left(\frac{r_e}{r_s}\right)^2\right], \quad (17)$$

$$\frac{d\phi_s}{d\xi} = -\frac{\delta}{r_s^2} + \frac{3}{4}\gamma\psi_{s0}^2 + \frac{2\Gamma}{f_p}\left(\frac{r_e}{r_s}\right)^2\left[2 - \left(\frac{r_e}{r_s}\right)^2\right], \quad (18)$$

where $r_e^{-2} = r_s^{-2} + r_{p0}^{-2}/f_p$, with $f_p = \cos^2(\xi) + C_p^2\sin^2(\xi)$. These ordinary differential equations (ODEs) can be solved numerically much faster than Eq. (9), which governs the evolution of the signal beam. However, the accuracy of the resulting solution needs to be checked by solving Eq. (9) directly.

We solve the coupled ODEs (15)–(18) with the fourth-order Runge-Kutta method and obtain the evolution of four beam parameters under different conditions. We check the accuracy of the solution by solving Eq. (9) numerically with the standard split-step Fourier method. The step size is 10^{-3} along the ξ axis and 10^{-2} in the transverse directions. In all cases, we employ the same values for the three parameters: $\gamma = 1 \times 10^{-4}$, $\Gamma = 5.7 \times 10^{-3}$, and $G_R = 3.5 \times 10^{-3}$. These are estimated using the following realistic values for a GRIN fiber: $a = 50$ μm and $\Delta = 0.01$, making $b = 2.83 \times 10^3$ m^{-1}. The input pump power is taken to be $P_{p0} = 0.1$ MW and the signal power P_{s0} is 1% of P_{p0}. The input beam has a Gaussian shape such that $\psi_s(r) = \psi_{s0}\exp(-r^2/2r_s^2 + id_s r^2 + i\phi_s)$ with the initial values $\psi_{s0} = 1$, $r_s = 1$, $d_s = 0$, and $\phi_s = 0$. Figure 2 compares the variational and numerical results over a propagation distance that corresponds to nine self-imaging periods ($\xi = 9\pi$). Excellent agreement between the numerical and variational results is evident in Fig. 2 over this distance. In Figs. 2(a i) and 2(a ii) we show the three-dimensional (3D) evolution of the signal beam and its x projection.
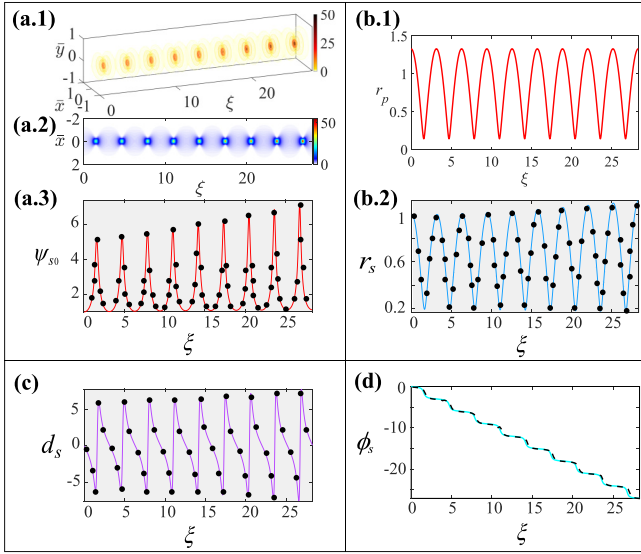
FIG. 2. Comparison between the variational (solid lines) and numerical (closed circles and dashed curves) predictions. (a i) Evolution of the signal beam inside the GRIN fiber, (a ii) signal beam's x projection, (a iii) signal's amplitude, (b i) pump's width, (b ii) width of the signal beam, (c) signal beam's phase-front curvature, and (d) signal beam's phase. The parameter values used were $\mu = 0.001$, $w_{s0} = 14.34$ μm, and $w_{p0} = 19$ μm.

FIG. 3. (a)–(c) Evolution of three signal-beam parameters ψ_{s0}, r_s, and d_s over a distance of 40 cm ($\xi = 1100$) using $r_{p0} = 1.33 r_{s0}$ without the nonlinear effects ($\gamma = \Gamma = 0$). Top rows in (a)–(c) compare the variational (solid line) and numerical (dashed line) results on a magnified scale. (d) Changes in the average width $\langle r_s \rangle$ of the signal with distance for four values of μ.

IV. IMPACT OF SPM AND XPM

Since the variational method predicts accurately the signal beam's dynamics under Raman amplification, we use it to study all possible scenarios for the signal's input width: (i) The signal beam is narrower than the pump beam ($w_{s0} < w_{p0}$), (ii) the signal beam is wider than the pump beam ($w_{s0} > w_{p0}$), and (iii) the signal beam is equal to the pump beam ($w_{s0} = w_{p0}$). We use realistic values for all other parameters.

A. Case of $w_{s0} < w_{p0}$

Assuming $w_{p0} = 1.33 w_{s0}$, we solve Eqs. (15)–(18) with and without including the SPM and XPM effects. Exploiting the variational results in Eqs. (15)–(18), it is possible to obtain an equation for the beam width r_s under certain approximations. For example, in the absence of SPM, r_s satisfies the differential equation

$$\frac{d^2 r_s}{d\xi^2} = -r_s + \frac{\delta^2}{r_s^3} - \mathcal{K}_\Gamma r_s \mathcal{F}^2(r_s) + \mathcal{K}_{G_R} r_s^3 \mathcal{F}^3(r_s) f_p'$$
$$- 2\mathcal{K}_{G_R} r_s^2 \mathcal{F}^3(r_s) f_p \frac{dr_s}{d\xi}, \tag{19}$$

where $\mathcal{F}(r_s) = (f_p r_{p0}^2 + r_s^2)^{-1}$, $\mathcal{K}_\Gamma = 4\delta\Gamma r_{p0}^2$, $\mathcal{K}_{G_R} = G_R r_{p0}^4$, and $f_p' = df_p/d\xi$. In obtaining this equation, we neglect a higher-order term associated with G_R because it has a negligible contribution. In the absence of XPM ($\Gamma = 0$) and Raman gain ($G_R = 0$), we set $\mathcal{K}_\Gamma = 0$ and $\mathcal{K}_{G_R} = 0$. This case was studied recently [16] and it was found that the width satisfies a simple equation $\frac{d^2 r_s}{d\xi^2} + r_s = \delta^2 r_s^{-3}$ and has the analytic solution $r_s(\xi) = [\cos^2(\xi) + \delta^2 \sin^2(\xi)]^{1/2}$.
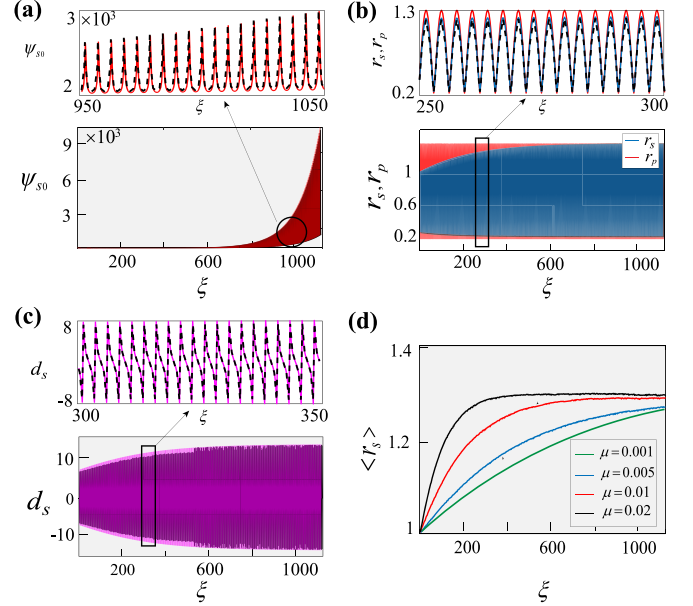
The last three terms in Eq. (19) result from the Raman amplification and the nonlinear effects such as the SPM and XPM and offers significant physical insight into the signal beam's evolution in a nonlinear GRIN-fiber amplifier. For example, the term containing $\mathcal{K}_\Gamma$ and related to the XPM is found to modulate the envelope of the GRIN-induced rapid periodic oscillations of r_s. The amplitude of this modulation is damped under the influence of the last term in Eq. (19). Finally, the term related to the Raman gain and containing $\mathcal{K}_{G_R}$ saturates the amplitude of rapid oscillation towards the initial pump width r_{p0}.

Following [16], we define the dimensionless parameter $\mu = g_R I_{p0} w_{s0}^2 / 2b w_{p0}^2$ that is controlled mainly by the input pump intensity (or power). For silica-based GRIN fibers, the Raman gain coefficient is $g_R = 1 \times 10^{-13}$ m/W at wavelengths near 1 μm. At an input pump power of 115 kW, the peak intensity is close to 100 TW/m². Its use yields $\mu = 0.001$ and $C_p = 0.1$ for $r_{p0}/r_{s0} = 1.33$. Such high-power values can be realized when the pump is in the form of nanosecond pulses.

To study the effect of Raman gain, we set $\Gamma = 0$, $\gamma = 0$, $\delta = 0.2$, and $\mu = 0.001$ and solve Eqs. (15)–(18); the results are presented in Fig. 3. As expected, the Raman gain amplifies the signal such that its amplitude in Fig. 3(a) exhibits an oscillatory pattern, seen clearly in the magnified view on top. In Fig. 3(b) the signal's width follows the same periodic self-imaging pattern as the pump width r_p (shown in red). This periodic self-imaging occurs for any GRIN fiber. The black dotted lines in the insets are obtained from numerical simulations; the variational results show excellent agreement with them. In the zoomed-in version in Fig. 3(b), the signal's width is larger than the pump's width at the point of maximum
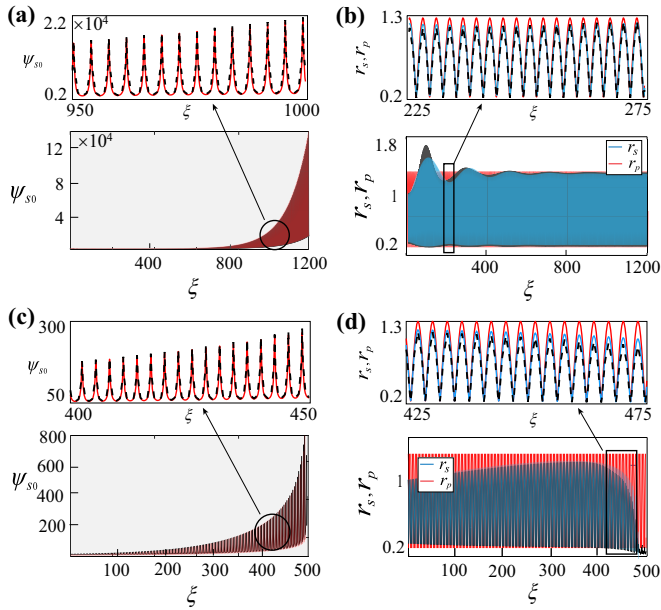
FIG. 4. Evolution of two parameters of the signal beam (ψ_{s0} and r_s) with (a) and (b) XPM only ($\gamma = 0$) and (c) and (d) SPM only ($\Gamma = 0$) for $r_{p0} = 1.33 r_{s0}$, i.e., $w_{s0} < w_{p0}$ for a distance $\xi = 1100$ ($z \approx 40$ cm). The insets show the oscillatory pattern on a magnified scale. The dashed lines in all the insets show numerical results obtained by solving Eq. (9).

FIG. 5. (a)–(c) Evolution of signal's parameters for $r_{p0} = 1.33 r_{s0}$ using $\gamma = 1 \times 10^{-4}$ and $\Gamma = 6 \times 10^{-3}$. (d i) Evolution of $\langle r_s \rangle$ with (oscillatory) and without XPM. The solid lines show the solution of Eq. (19) and dashed lines show numerical results. (d ii) Impact of SPM and XPM on of the average signal width $\langle r_s \rangle$. Evolution is shown without nonlinear effects (green solid line), with XPM only (red solid line), with SPM only (black solid line), and with both SPM and XPM (violet solid line). The last case is compared with numerical simulations using a blue dashed line.

compression where the effect of the pump on the signal is most prominent. To visualize changes in the signal's width more clearly, we plot in Fig. 3(d) its average value $\langle r_s \rangle$ as a function of ξ for four μ values. The average width is calculated by averaging r_s over several self-imaging periods ξ_p. It gradually increases with ξ and saturates at a value close to the pump's width for large ξ. The rate of increase depends on the value of μ and is larger for its larger values.

To investigate the individual effects of XPM and SPM on the evolution of signal beam, we consider two situations: (a) $\Gamma \neq 0$ and $\gamma = 0$ and (b) $\Gamma = 0$ and $\gamma \neq 0$. We solve the set of coupled ODEs (15)–(18) in both cases. The results for the evolution of the signal's amplitude and width are presented in Figs. 4(a) and 4(b) for the first case ($\Gamma = 5.7 \times 10^{-3}$ but $\gamma = 0$) and in Figs. 4(c) and 4(d) for the second case ($\Gamma = 0$ but $\gamma = 1 \times 10^{-4}$). In both cases, the signal's amplitude increases with a pattern similar to that found in Figs. 4(a) and 4(c). However, the signal's width exhibits unique features in Figs. 4(b) and 4(d). In the presence of XPM, the peak value of the signal's width undergoes oscillations before reaching a stable value. On the other hand, the presence of SPM leads to the beam's collapse due to self-focusing, as is evident in Fig. 4(d). To summarize, while Raman gain contributes to the signal beam's amplification and also changes its width, XPM leads to oscillations in the signal's width and SPM produces the beam's collapse owing to the self-focusing. Finally, we investigate the realistic case in which all three parameters G_R, Γ, and γ have finite values by solving Eq. (9) and the variational equations; the results are presented in Figs. 5(a)–5(c). As can be seen in Fig. 5(d ii), the average width $\langle r_s \rangle$ of the signal evolves in an oscillatory fashion, similar to that of a damped harmonic oscillator. When both SPM and XPM are
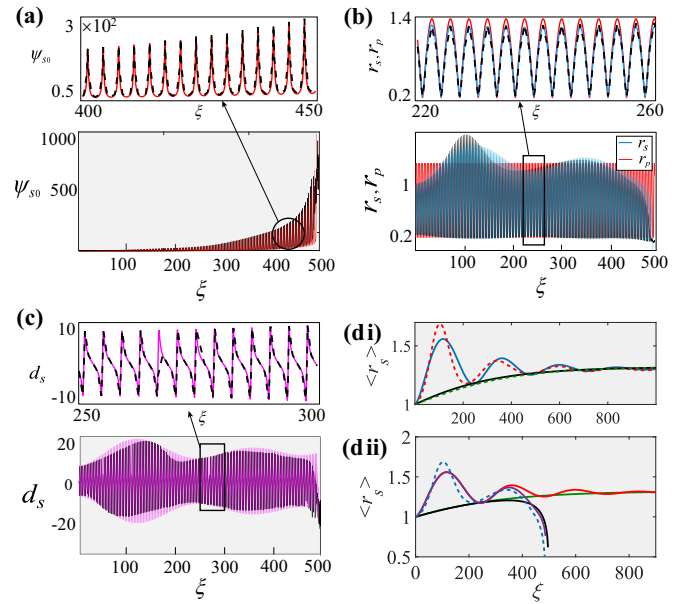
neglected, $\langle r_s \rangle$ increases monotonically towards a saturated value, as shown by the green solid line. When only XPM is included (red solid line), $\langle r_s \rangle$ exhibits damped oscillation and its value saturates near the pump's width, without any beam collapse. However, we observe a beam collapse only when SPM is included (black solid line) without any oscillations. When both XPM and SPM are included, $\langle r_s \rangle$ oscillates initially but eventually collapses (violet solid line) toward the value zero as the amplification of the signal beam increases its power toward the critical self-focusing power. It may appear surprising that a variational analysis does not break down near the self-focusing collapse. To verify its accuracy, we solve Eq. (9) and extracted numerically the values of $\langle r_s \rangle$. The results are shown in Fig. 5(d ii) by a blue dashed line and they validate the variational results.

Among the three nonlinear phenomena, the influence of SPM on the beam's dynamics is the most well known. The Raman gain and XPM are somewhat unique because the average beam width exhibits damped oscillations for them. To understand this unique feature, we employ Eq. (19) but ignore the influence of SPM, as we are more interested in the contributions of G_R and Γ. Given a relatively low value $G_R = 3.5 \times 10^{-3}$, the contribution of terms containing higher powers of G_R is also neglected. It is apparent from Eq. (17) that the phase-front curvature d_s varies in an oscillatory fashion when XPM is included, which influences the beam's width and produces oscillations in $\langle r_s \rangle$. Solutions of Eq. (19) with and without Γ are presented in Fig. 5(d i); they are in good agreement with the full numerical results (dashed line).
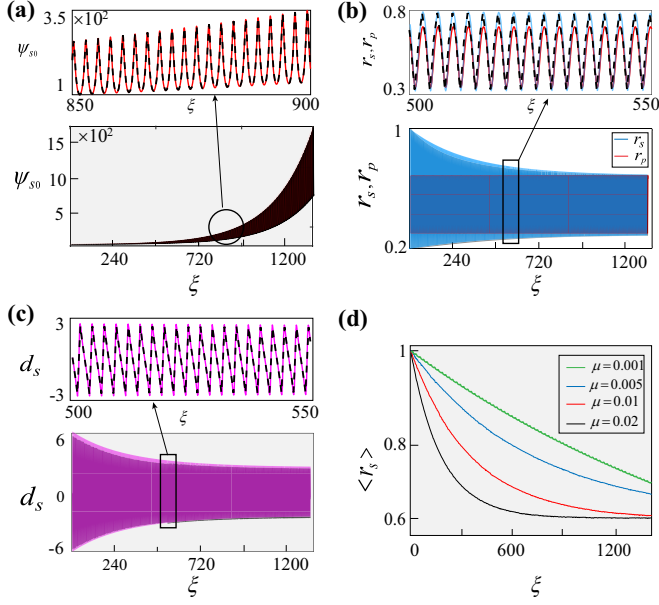
FIG. 6. Variational and numerical solution for the signal's parameters without the XPM and SPM effects ($\gamma = \Gamma = 0$) when $w_{s0} > w_{p0}$ ($r_{p0} = 0.67 r_{s0}$). The results are shown in the same format used for Fig. 3. The evolution of three parameters, (a) amplitude, (b) width, and (c) phase-front curvature, is shown. (d) Change of the average width $\langle r_s \rangle$ with ξ for different values of μ. The top panels in (a)–(c) compare the variational results (solid lines) with full numerical simulations (dashed lines).

B. Case of $w_{s0} > w_{p0}$

In this section we consider the evolution of a signal beam when its initial width is greater than the pump's width. For this purpose, we choose $w_{p0}/w_{s0} = r_{p0}/r_{s0} = 0.67$ with $\mu = 0.01$, $C_p = 0.42$, and $\delta = 0.2$. For $\mu = 0.01$, the Raman gain coefficient has a value $G_R = 9 \times 10^{-3}$. In the absence of nonlinearity, the evolution of the signal parameters is shown in Fig. 6. In contrast to the previous case, Fig. 6(b) shows a gradual reduction in the width of the signal beam. This feature is seen better in Fig. 6(d), where we plot the average width $\langle r_s \rangle$ as a function of the distance for several values of μ. The rate of width reduction is found to be proportional to the value of μ.

In Fig. 7 we show the individual effects of XPM and SPM on the beam's amplitude and width. The values used for the XPM and SPM coefficients are $\Gamma = 1.4 \times 10^{-2}$ and $\gamma = 6.45 \times 10^{-5}$, respectively.

The evolution of the signal beam amplitude and width under the influence of XPM and SPM is shown in Figs. 7(a) and 7(b) and Figs. 7(c) and 7(d), respectively, where the full simulation results are superimposed with variational results. In both the cases, an enhancement in the signal amplitude is observed. Under the influence of XPM, we observe the familiar oscillation in beam width where SPM leads to a beam collapse. From the top inset plots it is evident that variational results (solid line) are is in excellent agreement with full numerical simulation (dashed line).

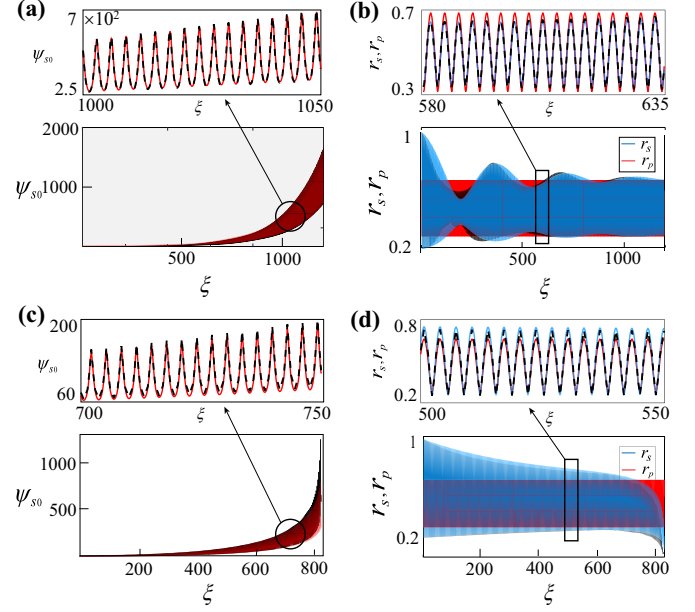In Fig. 8 we consider the full case by including both XPM and SPM simultaneously. Figure 8(a) shows the

FIG. 7. Evolution of two parameters of the signal beam (ψ_{s0} and r_s) with (a) and (b) XPM only ($\gamma = 0$) and (c) and (d) SPM only ($\Gamma = 0$) when $w_{p0} < w_{s0}$. Top panels show a magnified view and compare variational results (solid lines) with full numerical simulations (dashed lines).
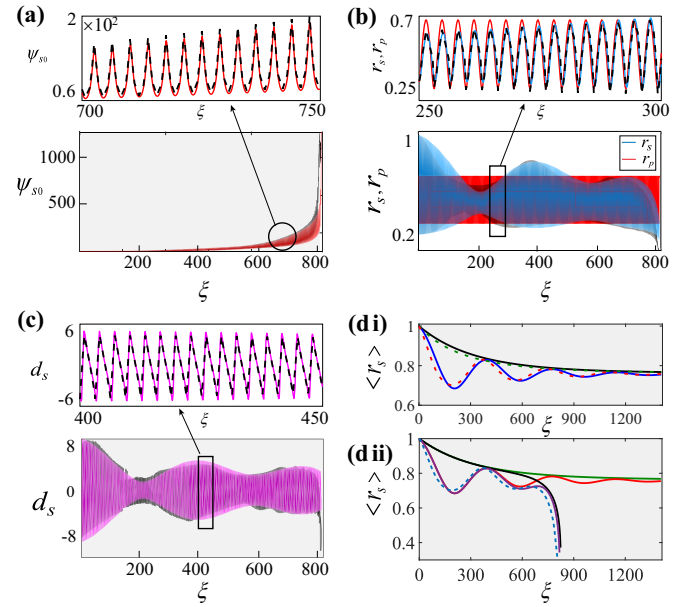

FIG. 8. Evolution of the signal's parameters in the case $w_{s0} > w_{p0}$ ($r_{p0} = 0.67 r_{s0}$) when both XPM and SPM effects are included: (a) amplitude, (b) width, and (c) phase-front curvature. The beam's collapse due to self-focusing is shown in (b). The variational results (solid lines) are compared with numerical simulations (dashed lines) in the top panel. (d i) Evolution of the signal's average width. Solid lines show the solution of Eq. (19) and dashed lines show numerical results. (d ii) Evolution of $\langle r_s \rangle$ in different regimes: without SPM and XPM (green solid line), with XPM only (red solid line), with SPM only (black solid line), and with both SPM and XPM (violet solid line). Numerical results for the last case are shown by a blue dotted line.
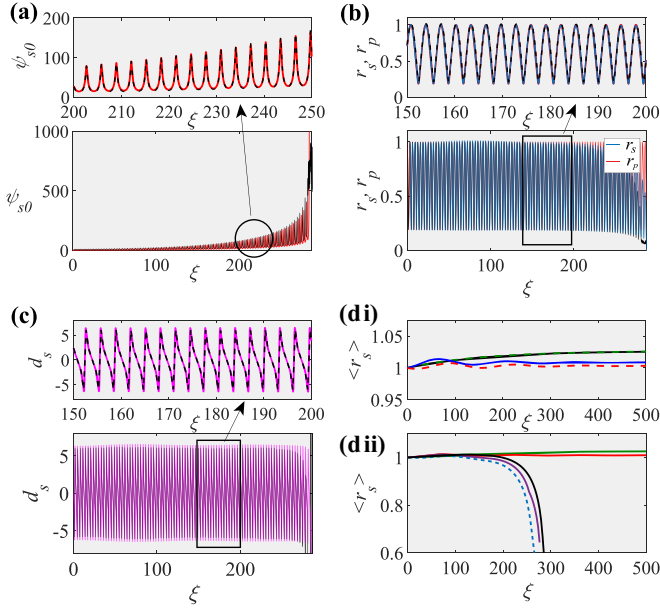
FIG. 9. Same as Fig. 8 but with $w_{p0} = w_{s0}$. Top panels in (a)–(c) compare variational results (solid lines) with full numerical simulations (dashed lines).

growth of the signal's amplitude using $\Gamma = 1.4 \times 10^{-2}$ and $\gamma = 6.45 \times 10^{-5}$. Changes in the widths of the signal and pump are shown in Fig. 8(b). Both widths follow an oscillatory pattern because of self-imaging inside a GRIN fiber. The phase-front curvature d_s also oscillates as shown in Fig. 8(c). Similar to Fig. 5, Fig. 8(d i) shows the evolution of the signal's average width $\langle r_s \rangle$ with and without XPM. Solid lines are obtained by solving Eq. (19) and the dashed lines show numerical results. Figure 8(d ii) shows the evolution of the average width $\langle r_s \rangle$ in four cases: without SPM and XPM (green solid line), with XPM only (red solid line), with SPM only (black solid line), and with both SPM and XPM (violet solid line). The width decreases monotonically when SPM and XPM effects are weak or ignored, exhibits damped oscillations when XPM is included without SPM, and experiences self-focusing collapse when only SPM is also included. Narrowing of the signal beam with increasing amplification expedites the self-focusing effect.

C. Case of $w_{s0} = w_{p0}$

For completeness of this study we also consider the specific case in which the pump and signal have the same width initially ($w_{s0} = w_{p0}$). Recall that the signal beam broadens when $w_{s0} < w_{p0}$ because of the Raman gain, but the exact opposite happens for $w_{s0} > w_{p0}$ when the nonlinear effects are ignored. When the XPM effects are included, the average width of the signal oscillates. Thus, when $w_{s0} = w_{p0}$ we expect negligible changes in the signal's width. The results shown in Fig. 9 support this expectation. Figure 9(a) shows that the beam's amplitude is amplified because of the Raman gain. Figure 9(a) shows that the beam's width oscillates because of self-imaging without much change in its peak value. The average width $\langle r_s \rangle$ shown in Fig. 9(d i) shows this feature more clearly. Similar to Fig. 8, Fig. 9(d ii) shows changes in
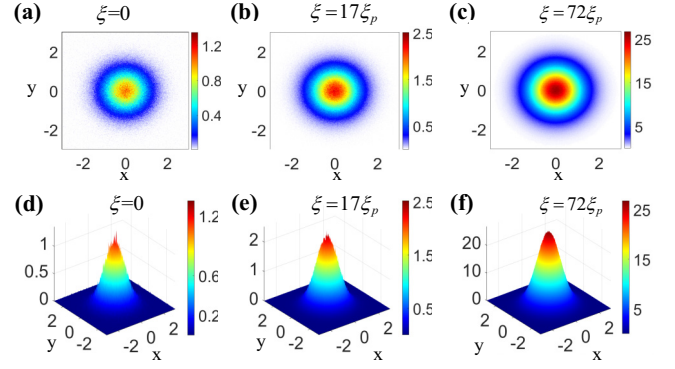

FIG. 10. Stability of a noisy Gaussian beam during its amplification inside a GRIN fiber. (a)–(c) Two-dimensional contour plots of the signal's intensity for three different distances using $r_{p0} = 1.33 r_{s0}$ without the XPM and SPM effects ($\gamma = \Gamma = 0$). (d)–(f) Corresponding 3D plots.

$\langle r_s \rangle$ with and without including the effects of SPM and XPM. Variational results again agree with full numerical simulations even when self-focusing collapse of the beam occurs.

D. Stability of the signal beam

The preceding analysis has been done under the assumption that the shape of the signal and pump beams remains Gaussian during their propagation inside the GRIN fiber. This is a fundamental requirement for any variational analysis. In recent works on Raman fiber amplifiers [6,7] and Kerr-induced beam cleanup in GRIN fibers [14], considerable reshaping of the beam can occur but the beam shape remains nearly Gaussian. To check for stability of the signal beam, we consider the evolution of an input Gaussian beam corrupted by noise by adding small random fluctuations to the amplitude of the input beam.

Figure 10 shows the intensity distribution at three different locations inside the GRIN fiber using contour plots [Figs. 10(a)–10(c)] and 3D plots [Figs. 10(d)–10(f)]. It is evident that random perturbations do not destroy the Gaussian nature of the beam during its propagation inside a GRIN-fiber amplifier. In fact, the beam becomes smoother as it propagates down the GRIN fiber. These results are indicative of the robustness of the Gaussian beams.

V. CONCLUSION

We have studied the Raman amplification of a signal beam inside a multimode graded-index fiber with a semianalytical variational approach, assuming that both the pump and signal are launched into the GRIN fiber in the form of cw or quasi-cw Gaussian beams. The variational analysis provides us with four coupled ordinary differential equations for the four relevant parameters (amplitude, width, phase, and phase curvature) that govern the evolution of the signal beam inside a GRIN fiber. These equations are much faster to solve numerically compared to the coupled nonlinear wave equation satisfied by the pump and signal beams. For context, a full numerical solution with acceptable accuracy for one set of input parameters typically takes more than 1000 times

more time compared to the solution of variational equations. Variational analysis also provides considerably more physical insight because it allows us to study the impact of important nonlinear phenomena such as SPM, XPM, and self-focusing in a controlled fashion.

We verified the accuracy of variational equations over a wide range of input parameters by comparing their solutions to the numerical predictions of the nonlinear wave equation governing the signal beam's evolution. More specifically, we used the variational equations to investigate the signal's evolution inside a GRIN Raman amplifier for different initial widths of the pump and signal beams. This allowed us to quantify the conditions under which the quality of a signal beam could be improved, without its collapse owing to self-focusing.

As expected, the widths of both the pump and signal beams undergo rapid periodic oscillations as a consequence of the self-imaging phenomena occurring in any graded-index fiber. The pump-induced XPM and the Raman gain is found to modulate the envelope of such oscillations for the signal beam. Because of Raman amplification, the XPM-induced modulation is damped in such a way that the average signal width approaches the pump's width at large distances.

Two conclusions can be drawn from the results given in this paper. First, in the absence of SPM, the Raman-gain-assisted narrowing of the signal beam can occur only when the input width of the pump beam is comparable to or smaller than that of the signal. As a result, Raman-induced beam cleanup is unlikely to occur in cladding pumped Raman amplifiers where the pump beam is always considerably wider than the signal beam. Second, one must avoid the collapse of the signal beam induced by self-focusing. In practice, this can be realized by decreasing the input signal power or the length of the GRIN fiber, to ensure that the signal's power remains below the critical power at which self-focusing leads to the beam's collapse.

While time-consuming numerical simulations may be needed when gain saturation and pump depletion must be included, the variational method is useful for two reasons. First, it can be used to scan the design parameters of an experiment in a time-efficient fashion and determine the optimum values of these parameters. Second, it can provide physical insight into the relative importance of different nonlinear phenomena involved in the Raman-amplification process.

[1] C. Jauregui, J. Limpert, and A. Tünnermann, Nat. Photon. **7**, 861 (2013).

[2] M. N. Zervas and C. A. Codemard, IEEE J. Sel. Top. Quantum Electron. **20**, 219 (2014).

[3] J. Zuo and X. Lin, Laser Photon. Rev. **16**, 2100741 (2022).

[4] S. H. Baek and W. B. Roh, Opt. Lett. **29**, 153 (2004).

[5] N. B. Terry, T. G. Alley, and T. H. Russell, Opt. Express **15**, 17509 (2007).

[6] N. B. Terry, K. Engel, T. G. Alley, T. H. Russell, and W. B. Roh, J. Opt. Soc. Am. B **25**, 1430 (2008).

[7] A. G. Kuznetsov, I. N. Nemov, A. A. Wolf, S. I. Kablukov, S. A. Babin, Y. Chen, T. Yao, J. Leng, and P. Zhou, J. Phys.: Conf. Ser. **1508**, 012009 (2020).

[8] O. S. Sidelnikov, E. V. Podivilov, M. P. Fedoruk, A. G. Kuznetsov, S. Wabnitz, and S. A. Babin, Opt. Express **30**, 8212 (2022).

[9] Y. Chen, T. Yao, H. Xiao, J. Leng, and P. Zhou, High Power Laser Sci. Eng. **8**, e33 (2020).

[10] Y. Chen, T. Yao, H. Xiao, J. Leng, and P. Zhou, J. Lightw. Technol. **39**, 1785 (2021).

[11] C. Fan, H. Xiao, T. Yao, J. Xu, Y. Chen, J. Leng, and P. Zhou, Opt. Lett. **46**, 3432 (2021).

[12] M. A. Jima, A. Tonello, A. Niang, T. Mansuryan, K. Krupa, D. Modotto, A. Cucinotta, V. Couderc, and S. Wabnitz, J. Opt. Soc. Am. B **39**, 2172 (2022).

[13] Z. Liu, L. G. Wright, D. N. Christodoulides, and F. W. Wise, Opt. Lett. **41**, 3675 (2016).

[14] K. Krupa, A. Tonello, B. M. Shalaby, M. Fabert, A. Barthélémy, G. Millot, S. Wabnitz, and V. Couderc, Nat. Photon. **11**, 237 (2017).

[15] G. P. Agrawal, Optical Fiber Technol. **50**, 309 (2019).

[16] G. P. Agrawal, J. Opt. Soc. Am. B **40**, 715 (2023).

[17] G. P. Agrawal, Opt. Lett. **48**, 259 (2023).

[18] G. P. Agrawal, *Nonlinear Fiber Optics*, 6th ed. (Elsevier, Amsterdam, 2019).

[19] M. Karlsson, D. Anderson, and M. Desaix, Opt. Lett. **17**, 22 (1992).

[20] D. Anderson, Phys. Rev. A **27**, 3135 (1983).

[21] S. Roy, S. K. Bhadra, and G. P. Agrawal, J. Opt. Soc. Am. B **26**, 17 (2009).

[22] D. Anderson, F. Cattani, and M. Lisak, Phys. Scr. **T82**, 32 (1999).